Quantification of Cerebral Blood Flow, Cerebral Blood Volume, and Blood–Brain-Barrier Leakage with DCE-MRI

Steven Sourbron,[1*] Michael Ingrisch,[1] Axel Siefert,[2] Maximilian Reiser,[3] and Karin Herrmann[3]

Dynamic susceptibility contrast MRI (DSC-MRI) is the current standard for the measurement of Cerebral Blood Flow (CBF) and Cerebral Blood Volume (CBV), but it is not suitable for the measurement of Extraction Flow (EF) and may not allow for absolute quantification. The objective of this study was to develop and evaluate a methodology to measure CBF, CBV, and EF from T1-weighted dynamic contrast-enhanced MRI (DCE-MRI). A two-compartment modeling approach was developed, which applies both to tissues with an intact and with a broken Blood-Brain-Barrier (BBB). The approach was evaluated using measurements in normal grey matter (GM) and white matter (WM) and in tumors of 15 patients. Accuracy and precision were estimated with simulations of normal brain tissue. All tumor and normal tissue curves were accurately fitted by the model. CBF (mL/100 mL/min) was 82 ± 21 in GM and 23 ± 14 in WM, CBV (mL/100 mL) was 2.6 ± 0.8 in GM and 1.3 ± 0.4 in WM. EF (mL/100 mL/min) was close to zero in GM (-0.009 ± 0.05) and WM (-0.03 ± 0.08). Simulations show an overlap between CBF values of WM and GM, which is eliminated when Contrast-to-Noise (CNR) is improved. The model provides a consistent description of tracer kinetics in all brain tissues, and an accurate assessment of perfusion and permeability in reference tissues. The measurement sequence requires optimization to improve CNR and the precision in the perfusion parameters. With this approach, DCE-MRI presents a promising alternative to DSC-MRI for quantitative bolus-tracking in the brain.   Magn Reson Med 62:205–217, 2009. © 2009 Wiley-Liss, Inc.

Key words: brain; perfusion; permeability; bolus-tracking; MRI

Dynamic Susceptibility-Contrast MRI (DSC-MRI) is the method of choice for the measurement of Cerebral Blood Flow (CBF) and Cerebral Blood Volume (CBV) with MRI (1). The method has proven highly successful in a variety of clinical applications (2), but despite a large amount of methodological research, absolute quantification remains a challenge (3–7).

A major source of error in DSC-MRI is the difference between blood and tissue relaxivity, which enters directly as a scaling error in the values of CBV and CBF, and has been estimated at a factor three for grey matter (8). Experimental data suggest that it depends on tissue type (9),

but this was not confirmed by simulation studies (10). It may also be different when the arterial signal is measured outside the vessel (2). An additional problem arises when the blood–brain-barrier (BBB) is broken. Extravasation of the contrast agent reduces the susceptibility contrast and amplifies the T_1-effects, which causes a signal increase that mimics tracer loss (11). For the measurement of CBF or CBV, T_1-interference may be minimized by data truncation (12) or corrected by modeling (13). It can be eliminated fully with a dual-echo sequence (14), but none of these approaches corrects for the loss in susceptibility contrast. No method has been proposed to minimize the error in the measurement of BBB-leakage itself (15–17).

This raises the question whether Dynamic Contrast-Enhanced MRI (DCE-MRI), which uses a T_1-weighted sequence to measure the bolus passage, is a more suitable approach when absolute quantification is required. DCE-MRI is the method of choice for the measurement of permeability (18–20), but CBV and CBF measurement is problematic because the signal changes induced by the intravascular component of the tracer are small (21). The problem originates from a combination of two factors: T_1-relaxivities (22) are an order of magnitude smaller than for T_2^* (8), and the small blood volumes in brain tissue (23) do not allow for large tissue concentrations. The small relaxivity does not impose a constraint on the measurement of permeability, because concentrations are higher if the tracer distributes over the much larger extravascular space.

On the other hand, DCE-MRI is not affected by the quantification issues typical to DSC-MRI: T_1-relaxivity of tissue equals that of arterial blood when the contrast agent is compartmentalized in the blood, and any possible T_2^*-interference is effectively negligible with typical echo times (1–2 msec). Also, a small number of studies have shown that CBV can be measured with DCE-MRI in normal brain tissue and infarction (24–26) and may be more accurate than DSC-MRI (27). The feasibility of measuring CBF, which requires a higher temporal resolution, has been demonstrated more recently (28,29). In tumors, where blood volumes are typically higher, CBV measurement is inherently less problematic (26), has equal diagnostic quality as DSC-MRI (30), and can be performed simultaneously with a measurement of permeability (31–33).

The first step towards a combined measurement of CBF, CBV, and BBB-leakage is taken in (34). Feasibility was evaluated in normal brain tissues and in tumors, but the data are acquired with a sampling time of 5.25 sec, which may be insufficient for CBF measurement (35). Also, the method combines two tracer-kinetic approaches with contradictory

205

assumptions (a one-compartment model and a model-free analysis), prior knowledge is required regarding the intactness of the BBB, and a one-compartment model may not fit tumor data with large blood volumes. Finally, a model-free analysis produces severe CBF errors in data with low SNR (36), though the error may be reduced by introducing appropriate constraints in the solution (29).

The aim of this study was to develop and evaluate a consistent and robust methodology for the measurement of CBF, CBV, and BBB-leakage with DCE-MRI. A tracer-kinetic model is proposed that produces all desired parameters with a single AIF, is designed to perform robustly in data with low SNR, and applies both to tissue with an intact and a broken BBB. The model was used to generalize DCE-MRI signal theory and incorporate potential differences in relaxivity between plasma and interstitium. The feasibility of the approach was evaluated using simulations of normal white matter (WM) and grey matter (GM) brain tissue, and data measured at 3T and at high temporal resolution in WM, GM, and brain tumors of 15 patients.

THEORY

Tracer-Kinetic Modeling of BBB-Leakage

A simple tracer-kinetic model that produces both blood flow and extraction flow is the *two-compartment exchange model* (37,38), illustrated in Fig. 1. It is fully defined by the four parameters F_P (plasma flow), V_P (plasma volume), F_E (extraction flow), and V_E (volume of the extravascular, extracellular space or interstitial volume, for short). Applying conservation of tracer mass to each compartment
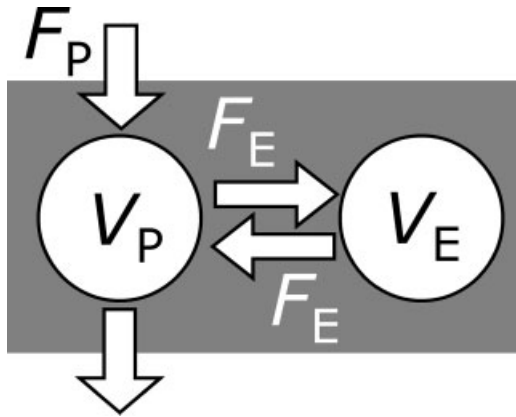

FIG. 1. Illustration of the two-compartment exchange model. It consists of a plasma compartment with volume V_E (left circle) and an interstitial compartment with volume V_E (right circle). The tracer first enters the plasma compartment carried by the plasma flow F_P. A fraction of the entering tracer is carried by the extraction flow F_E and enters the interstitial compartment. The tracer eventually leaves the interstitium through the reverse pathway, carried by a back flow of the same magnitude F_E. The uptake model is a three-parameter simplification of the exchange model which is defined by the assumption that backflow of tracer from the interstitium into the plasma compartment is negligible.

produces the model equations:

$$V_P C_P' = -F_E(C_P - C_E) + F_P(C_{P,A} - C_P) \quad [1]$$

$$V_E C_E' = +F_E(C_P - C_E) \quad [2]$$

Here we defined $C_{P,A}$, C_P, and C_E as the concentration in the arterial plasma, tissue plasma, and interstitium, respectively. Denoting the convolution product of two functions with the symbol "×" the solutions for C_P and C_E (37) can be written as $V_P C_P = F_P R_P \times C_{P,A}$ and $V_E C_E = F_P R_E \times C_{P,A}$. The functions R_P and R_E are given by the following expressions:

$$R_P(t) = e^{-tK_+} + T_B K_- E_-(e^{-tK_-} - e^{-tK_+}) \quad [3]$$

$$R_E(t) = (1 - T_B K_-)E_-(e^{-tK_-} - e^{-tK_+}) \quad [4]$$

The parameters K_+, K_-, and E_- are given by:

$$K_\pm = \frac{1}{2}\left(T_P^{-1} + T_E^{-1} \pm \sqrt{(T_P^{-1} + T_E^{-1})^2 - 4T_E^{-1}T_B^{-1}}\right) \quad [5]$$

$$E_- = \frac{K_+ - T_B^{-1}}{K_+ - K_-} \quad [6]$$

Here T_P and T_E are the mean transit times in both compartments, and T_B is the mean transit time of an intravascular tracer:

$$T_P = \frac{V_P}{F_E + F_P} \quad T_E = \frac{V_E}{F_E} \quad T_B = \frac{V_P}{F_P} \quad [7]$$

The total tissue concentration $C = V_P C_P + V_E C_E$ takes the form $C = F_P R \times C_{P,A}$ with a biexponential residue function $R = R_P + R_E$:

$$R(t) = e^{-tK_+} + E_-(e^{-tK_-} - e^{-tK_+}) \quad [8]$$

Fitting the model (Eq. [8]) to the data $C(t)$ and $C_{P,A}(t)$ produces the four parameters E_-, K_+, K_-, and F_P. The parameters T_P, T_E, T_B can then be calculated using the inverse of Eqs. [5,6]:

$$T_B^{-1} = K_+ - E_-(K_+ - K_-) \quad [9]$$

$$T_E^{-1} = T_B K_+ K_- \quad [10]$$

$$T_P^{-1} = K_+ + K_- - T_E^{-1} \quad [11]$$

Then the parameters V_P, V_E, and F_E can be found from the inverses of Eq. [7]:

$$V_P = F_P T_B \quad F_E = F_P\left(\frac{T_B}{T_P} - 1\right) \quad V_E = F_E T_E \quad [12]$$

The exchange model has three different monoexponential regimes: the no-exchange limit $F_E \rightarrow 0$, the one-compartment limit $V_E \rightarrow 0$, and the fast-exchange limit or flow-limited regime ($F_E \rightarrow \infty$). As a result, the model has three solutions with one redundant parameter when applied to tissue where the BBB is intact ($F_E = 0$).

The *two-compartment uptake model* is designed to overcome this redundancy in the solution. It is a simplification of the two-compartment exchange model, defined by the approximation $C_E(t) \ll C_P(t)$. Using the approximation

$C_E \ll C_P$ in Eqs. [1,2] we find the following set of model equations:

$$V_P C_P' = -F_E C_P + F_P(C_{P,A} - C_P) \qquad [13]$$

$$V_E C_E' = +F_E C_P \qquad [14]$$

A model with the same mathematical structure has been used previously for the evaluation of animal tumor models (39,40). Solving the equations produces the following formulae for R_P and R_E (the equivalent of Eqs. [3,4]):

$$R_P(t) = e^{-t/T_P} \qquad [15]$$

$$R_E(t) = E(1 - e^{-t/T_P}) \qquad [16]$$

Here E is the *exchange fraction*:

$$E = \frac{F_E}{F_E + F_P} \qquad [17]$$

The residue function for the two-compartment uptake model is given by $R_P + R_E$:

$$R(t) = e^{-t/T_P} + E(1 - e^{-t/T_P}) \qquad [18]$$

The model is fully defined by the three parameters F_P, T_P, E, and has only one monoexponential limit ($E = 0$). V_P and F_E can be found from:

$$F_E = \frac{EF_P}{1 - E} \quad V_P = \frac{T_P F_P}{1 - E} \qquad [19]$$

Hence the two-compartment uptake model allows to measure F_P, V_P, and F_E, but not V_E. This distinguishes it from the more conventional three-parameter two-compartment model (41), which produces V_E, F_E, and V_P, but not F_P.

In the context of this article, the introduction of the uptake model is mainly motivated by the need to avoid parameter redundancy for intact brain tissue (see above). However, it may also be useful in tissue with a broken BBB when the tracer extravasates very slowly, or when the acquisition time is so short that C_E never reaches high values. In this case, the duration of the transit through the interstitium (or the parameter T_E) may not be measurable. Fitting such data with the exchange model might introduce a parameter redundancy with a large variability in the values.

Relaxation in the Presence of BBB-Leakage

A major problem with DSC-MRI in the presence of leakage is that the signal changes are not only determined by the total concentration, but also by the manner in which this is distributed between intra- and extravascular space (11). A related problem arises with DCE-MRI when intra- and extravascular relaxivities are different. In this section, we evaluate how this affects the measured parameters.

We assume that the water-exchange across the cell walls is in the fast-exchange limit (42). Then the blood (*B*) and the extravascular tissue (*T*) are each characterized by a single longitudinal relaxation rate: $R_{1,B}$ and $R_{1,T}$, respectively. Assuming that the transendothelial water exchange is in the fast-exchange limit (43), the longitudinal relaxation rate

R_1 of the tissue ROI has the following form (we use the notation V_B for the CBV of the ROI):

$$R_1 = V_B R_{1,B} + (1 - V_B)R_{1,T} \qquad [20]$$

If a significant violation of the fast-exchange assumption cannot be excluded (43), the signal analysis may need to be refined and an additional measurement of the water exchange rate must be made (42). For the purposes of this study, we follow the conventional approach in DCE-MRI and assume that the effect is small (29,38).

Assuming that $R_{1,B}$ and $R_{1,T}$ are linearly related to the concentration in each space, we find:

$$R_1 = V_B(R_{10,B} + r_B C_B) + (1 - V_B)(R_{10,T} + r_T C_T) \qquad [21]$$

The sum $V_B R_{10,B} + (1 - V_B)R_{10,T}$ forms the precontrast relaxation rate R_{10}. Also, as the tracer is extracellular, we can set $V_B C_B = V_P C_P$ and $(1 - V_B)C_T = V_E C_E$:

$$R_1 = R_{10} + r_B V_P C_P + r_T V_E C_E \qquad [22]$$

We can now insert Eqs. [3,4] or Eqs. [15,16] to relate the change in tissue relaxation rate $\Delta R_1 = R_1 - R_{10}$ to $C_{P,A}(t)$:

$$\Delta R_1 = (r_B R_P + r_T R_E) \times F_P C_{P,A} \qquad [23]$$

Finally, we define $\Delta R_{1,A}$ as the change in relaxation rate of the arterial blood, and use the notation F_B for the CBF of the ROI. As $\Delta R_{1,A}/r_B$ is the concentration in the arterial blood, and the tracer is extracellular, we have:

$$F_P C_{P,A} = F_B \frac{\Delta R_{1,A}}{r_B} \qquad [24]$$

Inserting Eq. [24] into Eq. [23], we find the general expression:

$$\Delta R_1 = \left(R_P + \frac{r_T}{r_B} R_E\right) \times F_B \Delta R_{1,A} \qquad [25]$$

For the uptake model, Eqs. [15,16] show that $R_P + \rho R_E$ has exactly the same form as Eq. [18], after the substitution $E \to \rho E$. Equivalently, Eqs. [3,4] show that $R_P + \rho R_E$ for the exchange model has the same form as Eq. [8], with the substitution $E_- \to E_-(\rho)$:

$$E_-(\rho) = (\rho + (1 - \rho)T_B K_-)E_- \qquad [26]$$

This result shows that the ratio $\rho = r_T/r_B$ enters as a weighting factor on the extravascular component of the signal. Unfortunately, ρ is grouped with the other model parameters, so it cannot be treated as an independent parameter and fitted from the data. Hence the model parameters can only be determined if the value of ρ is known. For the contrast agent Gd-DTPA, relaxivity differences between water and plasma are small (22), so that those between plasma and interstitial fluid may be assumed negligible. This relaxivity-weighting may, however, be significantly larger for protein-bound contrast agents such as Gd-BOPTA or MS-325. For the remainder of this text, we will assume that $\rho = 1$, so that $R_P + \rho R_E = R$ (Eqs. [8,18]).

DCE-MRI Signal and Partial Volume Correction

It remains to provide a relation between the changes ΔR_1 in relaxation rate (Eq. [25]) and the DCE-MRI signal changes $\Delta S = S - S_0$. For the purposes of this study, we will assume that the signal S is proportional to R_1, which is a good approximation for small enough concentrations. Assuming that T_2^* effects of the tracer are negligible at echo times near 1 msec, the proportionality is constant in time so that $\Delta S / S_0 = \Delta R_1 / R_{10}$. This leads to:

$$\Delta R_1 = R_{10} \frac{\Delta S}{S_0} \qquad [27]$$

As precontrast T_1-values are significantly different between artery and tissue, the values do not cancel out in Eq. [25]. Hence accurate quantification requires a T_1-measurement prior to contrast injection—even in the linear regime.

The quantity $\Delta R_{1,A}$ in Eq. [25] is the change in relaxation rate in the arterial blood. In theory, it can be determined from Eq. [27] with a signal measured in the lumen of the artery, but this is not practically feasible due to the small size of the arteries in the brain. A corrected expression for $\Delta R_{1,A}$ can be found by applying the principles leading to Eq. [21] on a ROI that includes a fraction V_A of the arterial blood, and a fraction $1 - V_A$ of vessel wall and surrounding tissue (T). As the concentrations in and around a (normal) vessel wall are smaller than in the lumen ($C_T \ll C_A$), and $V_A \approx 1$ for a carefully drawn region, we can assume that the term $(1 - V_A)C_T$ is negligible compared with $V_A C_A$ in Eq. [21]:

$$\Delta R_1 = r_B V_A C_A \qquad [28]$$

We now write the concentration C_A in the arterial blood as $\Delta R_{1,A} / r_B$ (as in Eq. [24]), and use Eq. [27] to replace ΔR_1:

$$\Delta R_{1,A} = V_A^{-1} R_{10} \frac{\Delta S}{S_0} \qquad [29]$$

The arterial blood fraction V_A can be measured if a large draining vein lies in the field of view, so that at least one voxel can be identified in its lumen. The concentration $C_V(t)$ in the venous blood is a convolution of C_A with a probability distribution $H(t)$ (44). As arterial and venous blood have the same relaxivity, we can replace this by:

$$\Delta R_{1,V} = H \times \Delta R_{1,A} \qquad [30]$$

As the venous region is partial-volume free, we can use Eq. [27] with the relaxation rate $R_{10,B}$ of blood to replace $\Delta R_{1,V}$ by measurable quantities. For $\Delta R_{1,A}$ we insert Eq. [29]. This leads to:

$$\frac{\Delta S_V}{S_{0,V}} = P_A H \times \frac{\Delta S}{S_0} \quad \text{with} \quad P_A = V_A^{-1} \frac{R_{10}}{R_{10,B}} \qquad [31]$$

The parameter P_A can be measured by a deconvolution of the venous relative signal enhancement with that in the arterial ROI, and integrating the impulse response function. Using P_A in Eq. [29] we find the following expression for $\Delta R_{1,A}$:

$$\Delta R_{1,A} = P_A R_{10,B} \frac{\Delta S}{S_0} \qquad [32]$$

This result shows that the precontrast relaxation rate of the arterial ROI need not be known. This is fortunate, as a T_1-measurement in a region containing an artery may be unreliable due to the rapidly flowing blood.

MATERIALS AND METHODS

Patients

As the study aims to demonstrate the feasibility of the methodology, a heterogeneous patient group was analyzed to achieve a maximal amount of physiological variability. The study was approved by the institutional review board and informed consent was obtained from all patients. Fifteen patients with primary tumors of the brain ($n = 4$) or brain metastases ($n = 11$) were included in the study. The primary tumors included meningiomas ($n = 3$) and lymphoma ($n = 1$). The metastases were produced by a melanoma ($n = 2$), small-cell bronchial carcinoma ($n = 4$), nonsmall-cell lung carcinoma ($n = 3$), breast carcinoma ($n = 1$), colon carcinoma ($n = 1$). Four patients were not treated before imaging, the others were treated with radiotherapy, operation, chemotherapy, or a combination of the above.

Data Acquisition

All measurements were performed on a 3T scanner (Tim Trio, Siemens Medical Solutions) with a standard head coil. DCE-MRI was planned on a precontrast T_2-FLAIR and was followed by a high-resolution T_1-weighted sequence.

DCE-MRI was performed with a linearly encoded 2D spoiled gradient-echo sequence with a nonselective saturation prepulse (Turbo-FLASH). Six axial slices were measured every 1.34 sec for 7 min with a voxel size of $1.875 \times 1.875 \times 3.5$ mm^3. One slice was placed through the base of the skull to measure the arterial input function in the internal carotid artery. Sequence parameters were: 128×128 matrix, 96 phase encoding steps, field of view 240×240 mm^2, echo time 1.34 msec, repetition time 223 msec, inversion time 120 msec, flip angle 15°, bandwidth 735 Hz/pixel, echo spacing 2.6 msec. Parallel imaging was performed using GRAPPA with acceleration factor 2 and 24 reference lines. The slice gap was adjusted to achieve optimal coverage, depending on the size of the lesion and/or the presence of multiple lesions.

The DCE-MRI sequence was started 10 sec before injection of the contrast agent. Two 0.05 mmol/kg doses of Gd-DTPA (Magnevist, Schering) were injected intravenously at 3 mL/sec, the second 60 sec after the first. Each bolus was followed by a saline flush of 30 mL injected at the same rate. The aim of this double injection was to reduce the peak concentration without sacrificing the benefit of a full dose. Smaller concentrations are known to minimize errors caused by signal nonlinearity (45) in the artery and by limited transendothelial water exchange in the tissue (43).

Precontrast T_1 was measured immediately before bolus injection by repeating the DCE-MRI sequence with 17 different inversion times. The range 70 msec–1 sec was scanned in steps of 100 msec, the range 1 sec–2 sec in steps of 250 msec, then three measurements at 2.5 sec, 3 sec and 5 sec. At the smaller inversion times, the number of averages was increased to reach a minimum scan time of 10 sec. The total acquisition time for the T_1-measurement was 3 min.
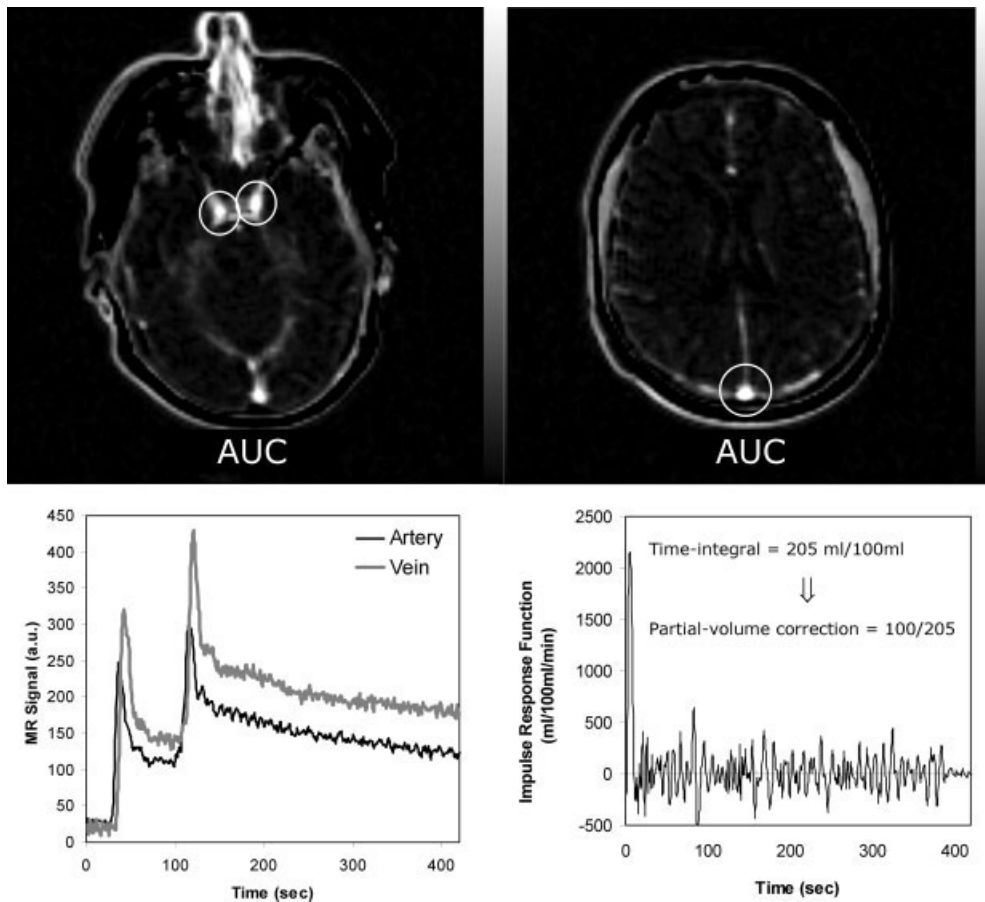
FIG. 2. Illustration of the arterial and venous data, and the method for determining the partial volume correction. The internal carotid arteries (top left) and the sinus sagittalis (top right) are easily identified on an image of the area under the signal enhancement curve (AUC). Circles are drawn manually around the vessels, and signals from the pixels with highest AUC within those circles are averaged to obtain arterial and venous curves (bottom left). Relative signal enhancement is calculated, and the venous outflow curve is deconvolved with the arterial input function (bottom right). The partial-volume correction factor is determined from the time-integral of the impulse response function.

Postprocessing

All data were transferred in DICOM format and processed off-line using the software PMI 0.3, written in-house in IDL 6.4 (ITT Visual Information Systems, Boulder, CO).

A map of the baseline signal S_0 was calculated as the mean of the first 15–20 dynamics. The background was segmented out semiautomatically by setting a threshold on the S_0 values, and disregarded in all subsequent calculations. The area under the signal enhancement curves ΔS (AUC) was calculated on the pixel level. A venous voxel was identified as the pixel in the sinus with the highest AUC. On the lowest axial slice of the AUC map, two circular ROIs were drawn manually around the internal carotid arteries (Fig. 2). The six pixels within those circles with maximum AUC were selected automatically, and their signal-time curves were averaged to extract the AIF. These steps were repeated for all data by two independent observers (S.S. and M.I.) to assess the reproducibility of this approach to AIF selection.

The impulse response function $P_A H(t)$ in Eq. [31] was determined by model-free deconvolution with generalized cross-validation (46) and integrated to produce the partial-volume correction factor P_A. An R_{10} map was calculated

by fitting the saturation-recovery data with variable delay times to a monoexponential. The change in tissue relaxation rate ΔR_1 was calculated for every voxel with Eq. [27]. $R_{10,B}$ was taken from the R_{10}-value in the venous voxel and $\Delta R_{1,A}$ was calculated with Eq. [32].

The data ΔR_1 and $\Delta R_{1,A}$ were fitted pixel-by-pixel to the uptake model (Eqs. [18,25]), producing maps of F_B, T_P, and E. To calculate the extraction flow F_E from Eqs. [19], the plasma flow F_P was calculated as $(1 - \text{Hct})F_B$ with a fixed hematocrit value of Hct = 0.45. A ROI covering the lesion was drawn manually on the F_E map and superposed on the F_B map to exclude areas of necrosis and larger blood vessels. Contralateral to the lesion, a circular white matter (WM) and grey matter (GM) ROI were defined on the map of the baseline signal S_0, superposed on the F_B map and shifted if necessary to exclude larger blood vessels.

The analysis was then repeated on the ROI level. The tumor ROI data were fitted both with the uptake model and with the exchange model (Eq. [8]), and the Akaike Information Criterion was used to select which of both models was most appropriate for the ROI data (47). Model selection was verified by visual inspection of the goodness-of-fit of both models. Model fitting was performed using MPFIT (48),
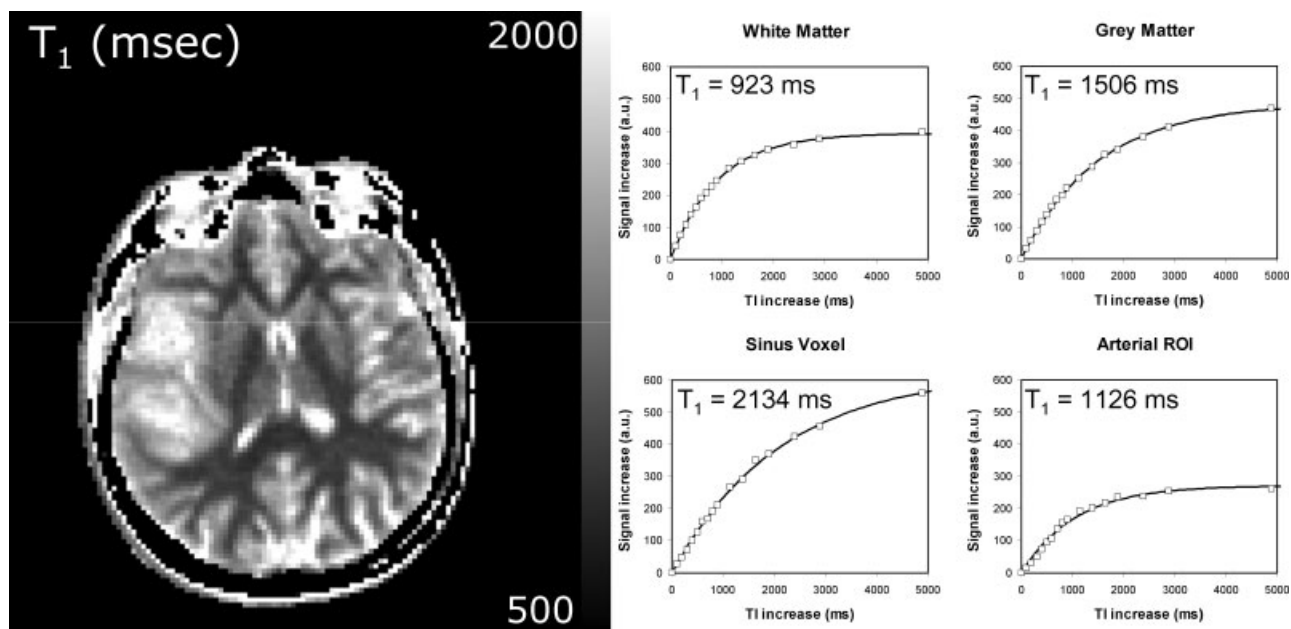
FIG. 3. An example of the results for the T1-measurement. On the left, a T1 map showing a large tumor on the right-hand side of the brain. On the right, data (squares) and model-fits (full line) for four reference regions: white matter, grey matter, a voxel inside the sinus sagitalis, and the region used to measure the arterial input function. The fitted T_1 value is displayed in the image.

with defaults for the number of iterations and convergence threshold, without constraints or limits on the parameters, and with analytical formulae for the partial derivatives. The initial values were fixed to $F_P = 120$ mL/100 mL/min, $F_E = 12$ mL/100 mL/min, $V_P = 10$ mL/100 mL, and $V_E = 20$ mL/100 mL.

Simulations

A simulated single-bolus AIF was generated by fitting a sum of gamma-variate functions and a mono-exponentially decaying recirculation to a typical measured AIF. A copy of this single-bolus AIF was shifted over 60 sec and added to the first to create a double-bolus AIF. Grey matter and white matter tissue curves were generated by convolving the AIF with a monoexponential impulse response function. CBF and CBV values for both tissue types were chosen to the mean values measured in the patient population (GM-WM: CBF 82–23 mL/100 mL/min, CBV 2.6–1.3 mL/100 mL/min, EF 0–0 mL/100 mL/min). All data were generated at a temporal resolution of 0.01 sec.

To simulate measurement, the data were first sampled at intervals of TR = 1.34 sec for a total acquisition time of 7 min (as in the measured data). Sampling was started at a time point t_0, which was determined by generating a random number uniformly distributed between $t = 0$ and $t = $ TR. To get a realistic estimate of the noise level, the fit to the uptake model in a typical GM and WM ROI curve was subtracted from the data to generate an approximate noise set. The Contrast-to-Noise Ratio (CNR), defined as the ratio of the maximum concentration to the standard deviation of the noise, was measured, producing a value of CNR = 4.1 for WM and CNR = 6.1 for GM. Normally distributed noise with the corresponding standard deviation was generated

and added to the data. The CNR in the AIF was estimated from a dataset and fixed to 130 for all simulations.

The simulated data were then fitted to the uptake model to produce an estimate of CBF, CBV, and F_E for typical GM and WM. The steps of simulated measurement and data fitting were repeated 10^5 times and a histogram was plotted of all parameters. Mean, standard deviation, and the main percentiles were determined as well. To investigate the effect of variable sampling times and of variable noise levels, the simulations were repeated for variable TR between 0.2 sec and 10 sec, and for variable CNR between 1 and 20.

RESULTS

Measurements

All measurements were performed without complications. In two patients no white matter or grey matter regions were defined, because the lesion and the slices were located in the cerebellum. Interobserver agreement in AIF selection was perfect: in each patient, both observers selected the same six arterial pixels.

Figure 2 illustrates the method of AIF selection and partial-volume correction in a typical case. The internal carotid arteries (top left) and the sinus sagittalis (top right) were always clearly identifiable on the AUC image. The impulse response function (bottom right) typically showed a single narrow peak, followed by a transient signal that fluctuates around zero. The partial volume correction factor P_A (Eq. [31]) covered a wide range from 0.40 to 1.0 with mean 0.69 (SD 0.20).

Figure 3 shows a typical result of the T_1-measurement on pixel and on ROI level. The images are smooth without outliers in the brain tissue, and white and grey matter regions are well differentiated. All data are well described
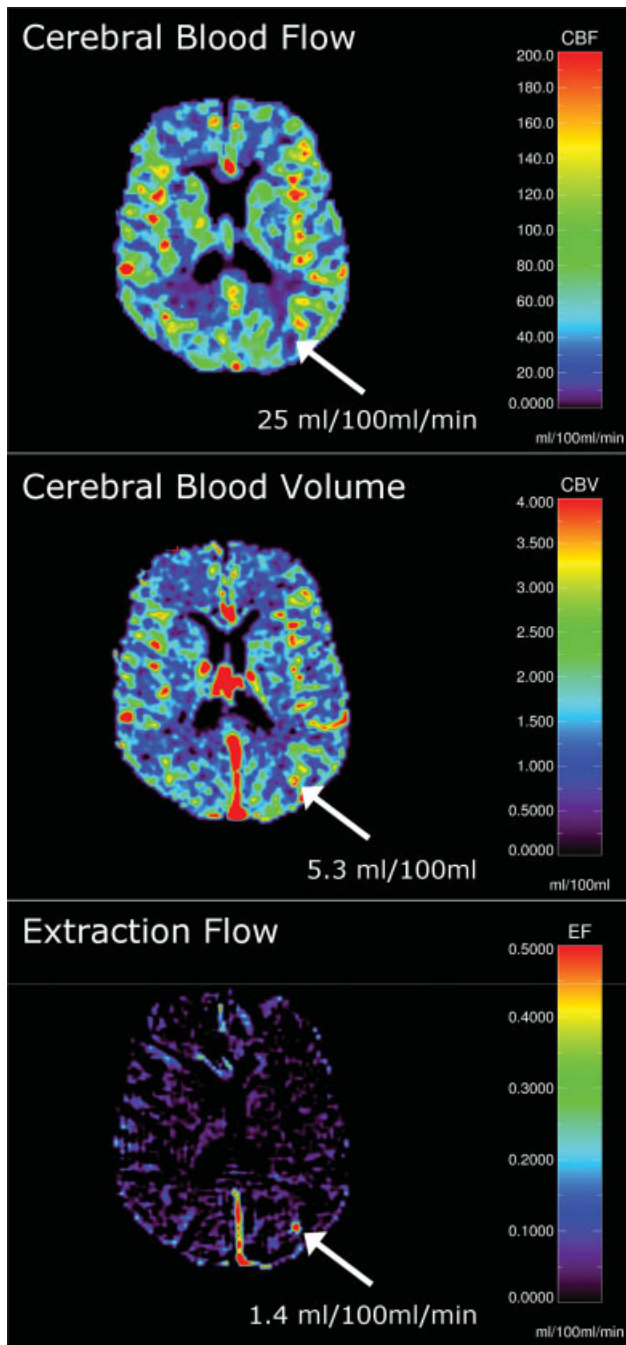
FIG. 4. An image of CBF (top), CBV (middle), and EF (bottom) calculated by fitting the pixel data to the two-compartment uptake model, with T_1 and partial-volume correction. The CBF map is median-filtered with a 3×3 window to remove salt-and-pepper noise. Data are shown for a patient with a metastasis of a nonsmall-cell lung carcinoma, after whole brain radiotherapy (18 Gy). A small lesion with a ruptured blood–brain-barrier is clearly identifiable on the EF-map (arrow). The lesion has an increased CBV, but a relatively low CBF in the white matter range.

by a monoexponential model, with the exception of those measured in the arterial ROI. Blood T_1-values are close to literature values (49), and ranged from 1,789 msec to 2,535 msec with mean 2,070 msec (SD 196). White matter T_1 ranged from 884 msec to 1,067 msec with mean 957 msec (SD 68). Grey matter T_1 ranged from 1,080 msec to 1,850

msec with mean 1,414 msec (SD 241). Tumor T_1 ranged from 1,020 msec to 2,882 msec with mean 1,733 msec (SD 411).

Figure 4 shows a typical result of a pixel-by-pixel analysis. Images of CBV and F_E are smooth with very few outliers, but a median filter must be applied on the CBF map to remove salt-and-pepper noise. Nevertheless, the resolution is sufficient to identify even small lesions. In general, lesions are most easily identified on the F_E maps and correspond in shape and location to those seen on the postcontrast T_1-map (not shown). Larger lesions often appear more heterogeneous on the maps of the blood flow or volume (see also Fig. 5). CBF and CBV values on the pixel level are in the appropriate range in normal tissue types and show good grey-to-white matter contrast.

Figure 5 shows a typical result of the ROI analysis for lesions (middle column) and normal tissue (right column). The tumor curves typically show a vascular peak with a steep signal increase, followed by a slower increase corresponding to the uptake phase, and by a washout phase with a negative slope. The bolus peak is visually clearly distinguishable in both WM and GM ROIs. The uptake model provided a good fit to the data in normal brain ROIs. It provided a close approximation to the tumor data, but a mismatch resembling oversmoothing was typically observed during the vascular peak of the bolus. The mismatch between model fit and data was reduced when the exchange model was applied, so that an additional parameter V_E was measurable. In one tumor ROI, a periventricular cerebral lymphoma, a wash-out was not observable and the exchange model did not visibly improve the fit to the data. The Akaike Information Criterion selected the uptake model as the best model in this case.

Figure 6 provides an overview of the three independent model parameters that were determined in all ROIs. CBF and CBV of all normal tissue regions were weakly positively correlated (pearson correlation coefficient 0.54). Table 1 shows the mean values and standard deviations of all parameters measured on ROI level.

Simulations

Figure 7 shows the histogram of the fitted parameter values for both tissue types. Open symbols display results for TR and CNR as in the patient data (CNR 4.1 for WM and 6.1 for GM). Closed symbols present results for an optimized sequence where CNR is increased by a factor 5. Note that, at the noise level of the measured data (open symbols) there is a strong overlap in WM and GM values of CBF and MTT, but not for CBV. With a fivefold increase in CNR, a complete separation between both tissue types can be achieved for all parameters.

Figure 8 illustrates the effect of variations in CNR and TR. The example depicts changes in CBF for GM. The WM results are similar. Note that changes in CNR and TR have very little effect on the accuracy of the results, but a reduction in CNR or temporal resolution severely reduces the precision of the measurement. The plots also illustrate that the precision is more effectively improved by increasing CNR than by a further reduction in TR. Quantitatively, a fivefold increase in CNR (see also Fig. 7) reduces the standard deviation in GM CBF from 21 to 3.9 mL/100 mL/min,
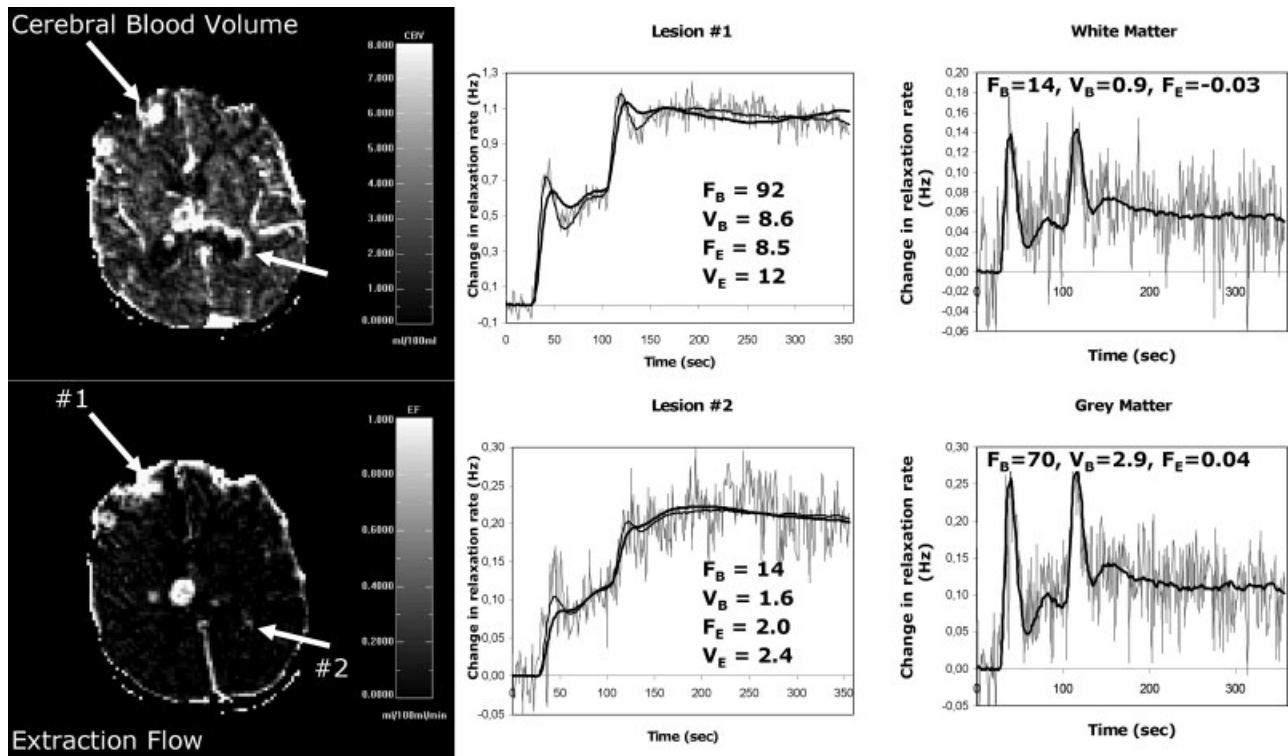
FIG. 5. An illustration of the results for one patient. The left column shows the blood flow and extraction flow maps. The plots in the middle column show the $\triangle R_1$ curves (thin grey line) and model fits (thick black line) for two regions: one in a lesion with high blood flow (lesion 1, top) and one with low blood flow (lesion 2, bottom). The positions of the lesions are indicated on the maps. The plots show best fits to the uptake model (thick black line) and to the exchange model (thin black line). Values displayed in the plot are produced by the exchange model. The plots in the right column are the results for the WM (top) and GM (bottom) tissue ROIs, fitted to the uptake model.

but a fivefold reduction in TR reduces the same standard deviation only to 8.5 mL/100 mL/min. Similar observations were made for the other parameters and for the WM data.

DISCUSSION

Tracer Kinetic Modeling

The uptake model provided a good fit to all data measured in normal brain tissue, which indicates that the well-mixedness of the vascular compartment is an appropriate assumption for DCE-MRI in the brain. A mismatch between the data and the fit to the uptake model was observed in most tumors. This is consistent with the assumption defining the model: when the measurement time increases, interstitial concentrations reach higher values, and the model becomes invalid. The mismatch is removed when the assumption is dropped and the more general exchange model is fitted (Fig. 5, middle). This indicates that the more fundamental assumptions underlying the model, the inclusion of no more than two compartments and the well-mixedness of a compartment, are sufficient for the modeling of DCE-MRI in the brain.

Hence the two-compartment model provides an alternative to a model-free deconvolution approach (29). Conceptually, the advantage of modeling is that it characterizes perfusion and permeability separately. This provides improved tissue characterization when the BBB is ruptured and the interpretation of the parameters does not

require prior knowledge regarding the state of the BBB. The modeling approach may also have a numerical advantage, because it constrains the number of degrees of freedom in the solution. Unconstrained model-free deconvolution is known to suffer from from low accuracy when the noise level is high (36). In (29) constraints are imposed by a polynomial representation of the residue function, which may be expected to improve accuracy and/or precision. The two-compartment model reduces the degrees of freedom in the solution to an absolute minimum ($n = 4$). Further simulation studies may allow to evaluate whether this provides additional numerical stability.

The two-compartment model also provides an alternative to the combination of two approaches for measuring perfusion and permeability: a deconvolution analysis with a measured AIF and a one-compartment model with a standardized AIF (34). Apart from possible inconsistencies due to the use of different AIFs, a potential problem is that both models contain conflicting assumptions. The one-compartment model assumes that the vascular space is negligible, whereas the deconvolution analysis assumes that it dominates. Also, the one-compartment model requires prior knowledge regarding the state of the tissue, because the interpretation of the parameters is different when the BBB is intact. Finally, as demonstrated by the data shown in this study, the vascular space in many tumors provides a significant contribution to the signal changes, in which case a one-compartment model does not accurately fit the data.
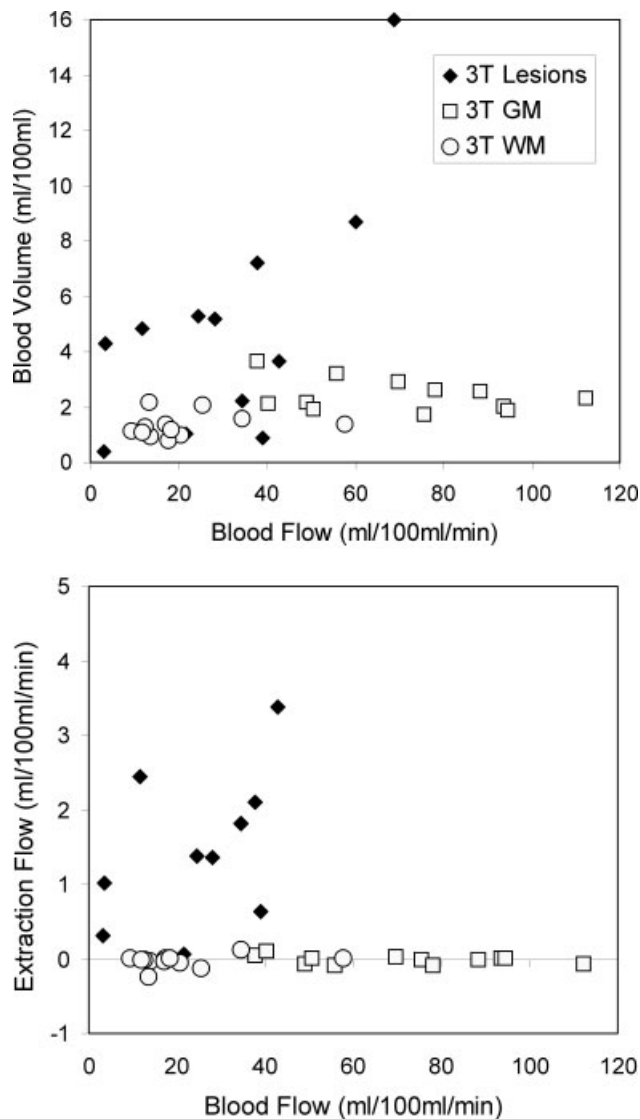
FIG. 6. A plot of both vascular parameters blood flow F_B and blood volume V_B (top) and of both flow parameters F_B and the extraction flow F_E (bottom) for all regions of interest. Symbol shapes refer to tissue type: lesions (diamond), grey matter (square), white matter (circle). One lesion with a high blood flow (141 mL/100 mL/min) is not plotted for reasons of clarity.

Accuracy and Precision

Typical GM CBF values measured by PET in normal volunteers (50) are lower than the mean values in this study (Table 1), but higher values have been reported as well (51). Our CBV values are in the range 2–5% determined ex-vivo in brain tissue (23), but most PET values report slightly higher values (50). Apart from uncertainties in the PET values, such discrepancies may also be due to the fact that the data in this study are not measured in a normal population. On the other hand, within the context of this feasibility study it cannot be excluded that systematic errors are present in the data. Nevertheless, the observation that all values in GM and WM are in the right order of magnitude shows that the methodology is sufficiently accurate to motivate further experimental studies.

Standard deviations of CBF are larger than other results found in the literature (29), and an overlap between white and grey matter CBF values was observed (Fig. 6). The same effects were observed in the simulations (Table 1, Fig. 7), which indicates that a large part of the variability in CBF is due to the noise in the data. Precision in CBF is improved significantly at higher CNR (Fig. 8) and separation between WM and GM is complete at noise levels closer to those in (29) (Fig. 7). This indicates that a higher CNR is required for applications that aim to quantify more subtle variations in tissue CBF.

Simulations show that CBV is a more precise parameter than CBF (Table 1), and that WM and GM are well separated on the basis of their CBV values (Fig. 7). Standard deviations in measured CBV are, however, larger than in simulations (Table 1), and the separation between WM and GM is less clear-cut than expected on the basis of the simulations (Fig. 6). This indicates that the observed variability in CBV reflects the heterogeneity of the population. As tumors exert pressure on the brain, and most patients in the study are undergoing some form of treatment, GM and WM tissue perfusion is likely to be more heterogeneous than that in a normal population.

The measured mean and standard deviations in the F_E values of intact brain tissue are very close to the expected value of zero (Table 1), which indicates that the permeability measurements are accurate and precise. The simulations also show that F_E is a very precise parameter, despite the low CNR in the data. A possible explanation is that F_E is estimated from the "tail" of the concentration-time curves, where concentrations change slowly, and which

Table 1
Mean Value and Standard Deviation of All Parameters Measured on ROI Basis: The Blood Flow F_B, the Blood Volume V_B, the Mean Transit Time of the Plasma Compartment T_P, the Extraction Flow F_E, the Interstitial Volume V_E, and the Interstitial Mean Transit Time T_E

Mean (std dev)	Lesion	Grey matter		White matter	
		Simulations	Measurements	Simulations	Measurements
F_B (mL/100 mL/min)	42 (40)	88 (28)	82 (21)	24 (7.9)	23 (14)
V_B (mL/100 mL)	8.9 (11)	2.6 (0.1)	2.6 (0.8)	1.3 (0.07)	1.3 (0.4)
T_P (sec)	12 (12)	1.9 (0.5)	2.1 (1.1)	3.5 (1.0)	4.4 (2.2)
F_E (mL/100 mL/min)	2.3 (2.2)	−0.0007 (0.01)	−0.009 (0.05)	−0.0003 (0.01)	−0.03 (0.08)
V_E (mL/100 mL)	8.2 (4.3)	N/A	N/A	N/A	N/A
T_E (sec)	297 (196)	N/A	N/A	N/A	N/A

Measured values are given for the lesions, for white matter and for grey matter. Simulated values for grey and white matter are given for comparison. The parameters V_E and T_E are produced by the exchange model which was only meaningful for the lesions.
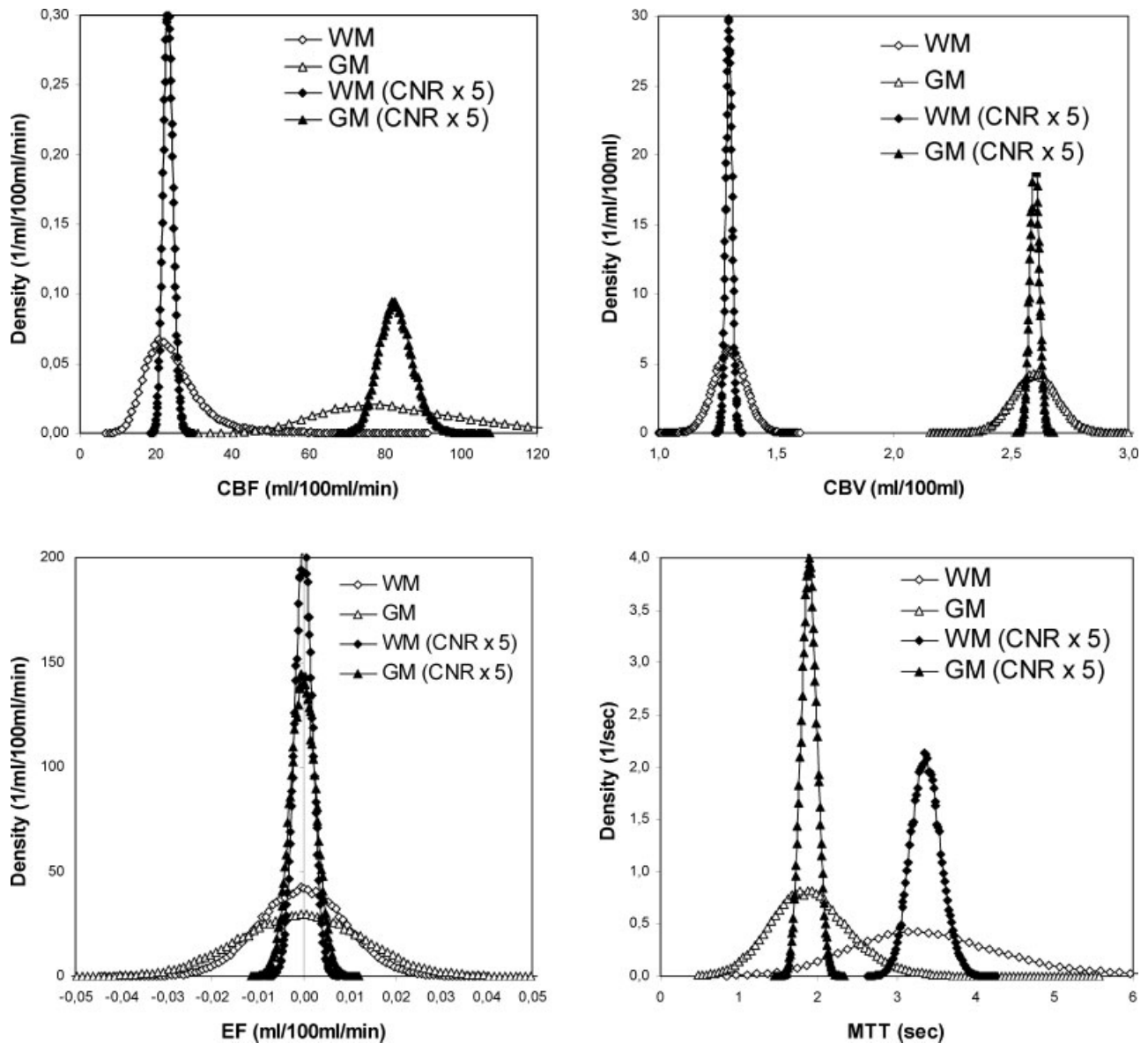
FIG. 7. Plots of the simulated histograms for CBF (top left), CBV (top right), EF (bottom left), and MTT (bottom right). The open symbols plots display the histograms for GM (◇) and WM (△) for CNR and TR equal to those measured in the patient data. The corresponding closed symbols (♦, ▲) give the histograms for an optimized sequence which leads to a fivefold increase in CNR.

are covered by a large amount of data points. Interestingly, the average F_E-values are slightly negative. The deviation from zero is an order of magnitude higher than the mean values in the simulations, and may therefore be attributed to a systematic effect. A possible explanation is a residual T_2^*-effect, despite the small echo times.

Extraction flow values in the tumor data cover a large range (Fig. 6), but the range of interstitial volumes (Table 1) agrees very well with estimates for typical tissue types (4–12%) (23). For the vascular parameters, one may expect that a measurement in tumors is at least as robust as in normal tissue: due to the higher blood volumes (Table 1), peak enhancement in the first pass is significantly higher than in normal tissue. On the other hand, not all lesions of interest are highly perfused. In particular, the characterization of

pure radiation effects requires high accuracy in the lower CBF- and CBV ranges (Fig. 6, top).

Protocol Optimization

Pixel-by-pixel analysis with the uptake model was feasible, but isolated pixels in which the algorithm converged to unphysiological values could be identified on the CBF map and needed to be removed by a median filter (Fig. 4). This observation is in apparent contradiction with previous studies showing accurate and precise CBF quantification on the pixel level (28,29). A comparison of the sequence parameters, however, reveals that the voxel size used in this study (12.3 mm³) is significantly smaller compared with those in previous studies (62 mm³ at 3T (29) and 211
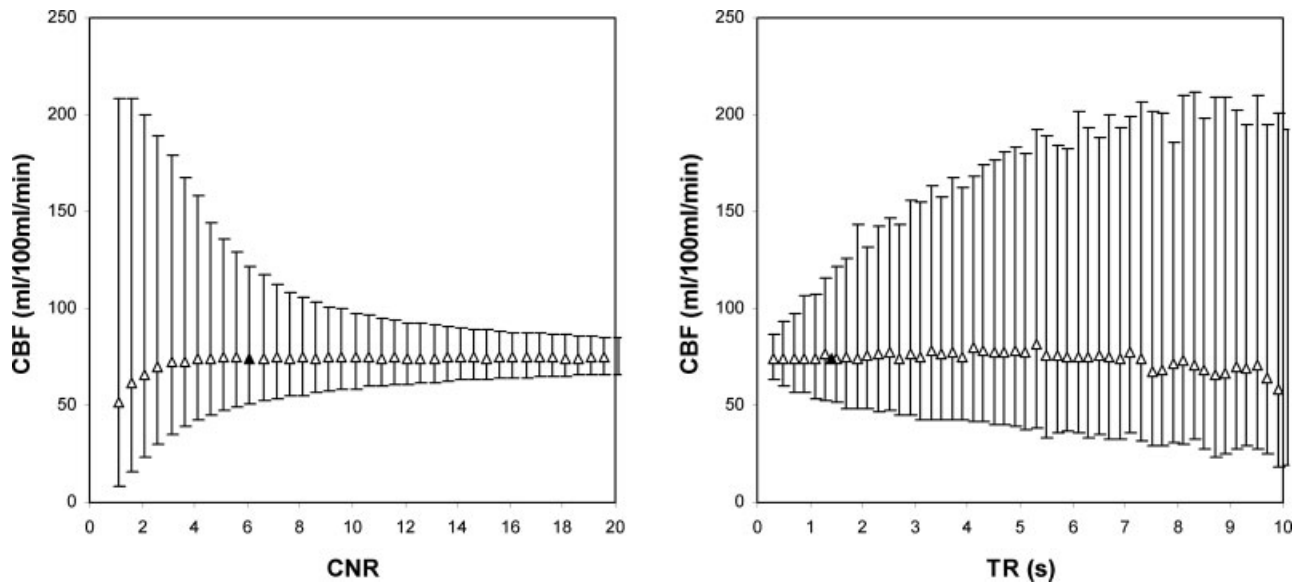
FIG. 8. Plots of the measured CBF values for GM at different values of CNR (left) and TR (right). The open symbols (△) correspond to the median values, error bars are plotted from the 5th to the 95th percentile. The single filled symbol (▲) corresponds to the CNR (6.1) and TR (1.34 sec) of the measured data.

mm³ at 1.5T (28)). Moreover, these studies have chosen to sacrifice coverage (29) and/or temporal resolution (28) for a smaller bandwidth. Many DSC-MRI studies also use a significantly higher voxel size, e.g., 30.3 mm³ (7) or 70.3 mm³ (13), though others use a voxel volume near to the one in this study (17.5 mm³ in (6)). Hence the CNR can be increased significantly by increasing the voxel volume to more typical values. Figure 7 shows that this has a very strong effect on the precision of the results and creates a clear-cut separation between WM and GM CBF.

The choice of the temporal resolution is generally considered to be a major issue for bolus-tracking MRI. Little theoretical or experimental evidence is available concerning the optimal choice for TR, but it is usually recommended that TR is not larger than 1.5 sec in the brain (35). Such recommendations are based on the intuition that TR must be smaller than the MTT of the tissue, so that the residue function is appropriately sampled. On the other hand, other authors have reported accurate CBF values for TR significantly larger than typical MTT values (34,52). The simulation results in Figure 8 provide some insight into these issues. The figure shows, first, that an increase in TR does not affect the accuracy of the solution, but only reduces the precision. Second, the precision is obviously improved at smaller TR, but there is no clear change in behavior near the MTT of the tissue. This implies that MTT does not impose a fundamental constraint, but that TR should be minimized as far as possible. In reality, however, a reduction in TR is accompanied by a reduction in CNR, so that an optimal trade-off between both measures should be sought. Future studies for particular imaging sequences are necessary to identify an optimum, but these results indicate that it may be advantageous to sacrifice temporal resolution for an improvement in CNR.

A major limitation of the current measurement protocol is the limited coverage. A six-slice acquisition does not cover the whole brain, which imposes limitations for the evaluation of multiple lesions (e.g., metastases, multiple sclerosis lesions), or of more diffuse pathologies such as ischemia. More slices can be acquired if the matrix size or the temporal resolution are reduced, but a coverage of 20 slices as typically used in DSC-MRI is not feasible within the current sequence. An alternative approach to improve the coverage is the use of a 3D sequence (52). Experience in other organs demonstrates that with this approach a volume of 20 slices can be acquired at a high temporal resolution (53). An additional advantage of the 3D approach is that a non-selective preparation pulse may not be necessary to minimize inflow effects (52). As the magnetization then is not destroyed before signal acquisition, this implies a significant improvement in CNR.

An important consideration for quantitative DCE-MRI in the brain is the choice of contrast agent dose. A high dose maximizes signal enhancement in the tissue, but may cause overestimation in CBF by signal saturation or nonlinearity in the artery (45), and underestimation due to transendothelial water exchange effects (43). The use of a prebolus eliminates arterial signal saturation (54), but not the effect of water exchange. For these reasons we proposed an alternative approach in the form of a double bolus injection. This reduces both sources of error by a reduction in peak concentration, without sacrificing the benefit of a full dose. The double bolus may also be helpful in detecting/correcting nonlinearity effects. Figure 2 shows no obvious signs of nonlinearity, but in other data sets the height of both peaks was nearly equal. This indicates that nonlinearity remains an issue, and the method might benefit from a more refined signal model.

CONCLUSION

The two-compartment uptake model presents a consistent and robust tracer-kinetic approach that applies both

to tissues with an intact as with a ruptured BBB. It provides a good fit to DCE-MRI data in intact brain tissue and accurate values for CBF, CBV, and BBB-leakage. A mismatch between data and model fit was observed in most tumors, which was removed by using the exchange model, producing an additional measurement of the interstitial volume. The precision in CBF was low with the current protocol, and a single-voxel analysis was not sufficiently robust at the high spatial resolution used in this study. Simulations suggest that the problem can be solved by sequence optimization and/or increasing the voxel size to more conventional values. After these improvements, DCE-MRI may allow for an accurate and precise characterization of perfusion and permeability in normal brain tissue and in brain lesions. As AIF selection is straightforward, and BBB-leakage effects are negligible or can easily be corrected for, DCE-MRI offers a suitable alternative to DSC-MRI for absolute quantification of bolus-tracking MRI in the brain.

ACKNOWLEDGMENTS

REFERENCES

1. Rosen BR, Belliveau JW, Vevea JM, Brady TJ. Perfusion imaging with NMR contrast agents. Magn Reson Med 1990;6:249–265.
2. Sorensen AG, Reimer P. Cerebral MR Perfusion Imaging. New York: Georg Thieme Verlag/Stuttgart; 2000.
3. Lin W, Celik A, Derdeyn C, An H, Lee Y, Videen T, Ostergaard L, Powers, WJ. Quantitative measurements of cerebral blood flow in patients with unilateral carotid artery occlusion: A PET and MR study. J Magn Reson Imag 2001;14:659–667.
4. Carroll TJ, Teneggi V, Jobin M, Squassante L, Treyer V, Hany TF, Burger C, Wang L, Bye A, Von Schulthess GK, Buck A. Absolute quantification of cerebral blood flow with magnetic resonance, reproducibility of the method, and comparison with H2(15)O positron emission tomography. J Cereb Blood Flow Metab 2002;22:1149–1156.
5. Chen JJ, Frayne R, Smith MR. Reassessing the clinical efficacy of two MR quantitative DSC PWI CBF algorithms following cross-calibration with PET images. Phys Med Biol 2005;50:1251–1263.
6. Knutsson L, Börjesson S, Larsson EM, Risberg J, Gustafson L, Passant U, Ståhlberg F, Wirestam R. Absolute quantification of cerebral blood flow in normal volunteers: Correlation between Xe-133 SPECT and dynamic susceptibility contrast MRI. J Magn Reson Imaging 2007;26:913–920.
7. Engvall C, Ryding E, Wirestam R, Holtas S, Ljunggren K, Ohlsson T, Reinstrup P. Human Cerebral Blood Volume (CBV) measured by dynamic susceptibility contrast MRI and ^{99m}Tc-RBC SPECT. J Neurosurg Anesthesiol 2008;20:41–44.
8. Kiselev VG. Transverse relaxation effect of MRI contrast agents: a crucial issue for quantitative measurements of cerebral perfusion. J Magn Reson Imag 2005;22:693–696.
9. Newman GC, Hospod FE, Patlak CS, Fain SE, Pulfer KA, Cook TD, O'Sullivan F. Experimental estimates of the constants relating signal change to contrast concentration for cerebral blood volume by T2* MRI. J Cereb Blood Flow Metab 2006;26:760–770.
10. Kjølby BF, Østergaard L, Kiselev VG. Theoretical model of intravascular paramagnetic tracers effect on tissue relaxation. Magn Reson Med 2006;56:187–197.
11. Sourbron S, Heilmann M, Biffar A, Walczak C, Vautier J, Volk A, Peller M. Tracer kinetic analysis of a simultaneous T1- and T2* measurement in a tumor model. In: Proceedings of the 16th Annual Meeting of the ISMRM, Ontario, Canada, 2008. p 2789.
12. Cha S, Knopp EA, Johnson G, Wetzel SG, Litt AW, Zagzag D. Intracranial mass lesions: Dynamic contrast-enhanced susceptibility-weighted echo-planar perfusion MR imaging. Radiology 2002;223:11–29.
13. Boxerman JL, Schmainda KM, Weisskoff RM. Relative cerebral blood volume maps corrected for contrast agent extravasation significantly

14. correlate with glioma tumor grade, whereas uncorrected maps do not. Am J Neuroradiol 2006;27:859–867.
14. Uematsu H, Maeda M, Sadato N, Matsuda T, Ishimori Y, Koshimoto Y, Yamada H, Kimura H, Kawamura Y, Matsuda T, Hayashi N, Yonekura Y, Ishii Y. Vascular permeability: Quantitative measurement with double-echo dynamic MR imaging—theory and clinical application. Radiology, 2000;214:912–917.
15. Johnson G, Wetzel SG, Cha S, Babb J, Tofts PS. Measuring blood volume and vascular transfer constant from dynamic, T2*-weighted contrast-enhanced MRI. Magn Reson Med 2004;51:961–968.
16. Law M, Young R, Babb J, Rad M, Sasaki T, Zagzag D, Johnson G. Comparing perfusion metrics obtained from a single compartment versus pharmacokinetic modeling methods using dynamic susceptibility contrast-enhanced perfusion MR imaging with glioma grade. Am J Neuroradiol 2006;27:1975–1982.
17. Bang OY, Buck BH, Saver JL, Alger JR, Yoon SR, Starkman S, Ovbiagele B, Kim D, Ali LK, Sanossian N, Jahan R, Duckwiler GR, Vinuela F, Salamon N, Villablanca JP, Liebeskind DS. Prediction of hemorrhagic transformation after recanalization therapy using T2*-permeability magnetic resonance imaging. Ann. Neurol., 2007;62:170–176.
18. Larsson HB, Stubgaard M, Frederiksen JL, Jensen M, Henriksen O, Paulson OB. Quantitation of blood–brain barrier defect by magnetic resonance imaging and gadolinium-DTPA in patients with multiple sclerosis and brain tumors. Magn Reson Med 1990;16:117–131.
19. Kermode AG, Tofts PS, Thompson AJ, MacManus DG, Rudge P, Kendall BE, Kingsley DP, Mosely IF, du Boulay EP, McDonald WI. Heterogeneity of blood–brain barrier changes in multiple sclerosis: An MRI study with gadolinium-DTPA enhancement. Neurology 1990;40:229–235.
20. Kassner A, Roberts T, Taylor K, Silver F, Mikulis D. Prediction of hemorrhage in acute ischemic stroke using permeability MR imaging. Am J Neuroradiol 2005;26:2213–2217.
21. Villringer A, Rosen BR, Belliveau JW, Ackerman JL, Lauffer RL, Buxton RB, Chao Y-S, Wedeen VJ, Brady TJ. Dynamic imaging with lanthanide chelates in normal brain: Contrast due to magnetic susceptibility effects. Magn Reson Med 1988;6:164–174.
22. Rohrer M, Bauer H, Mintorovitch J, Requardt M, Weinmann H-J. Comparison of magnetic properties of MRI contrast media solutions at different magnetic field strengths. Invest Radiol 2005;40:715–724.
23. Bassingthwaite JB. Micocirculatory considerations in NMR flow imaging. Magn Reson Med 1990;14:172–178.
24. Dean BL, Lee C, Kirsch JE, Runge VM, Dempsey RM, Pettigrew LC. Cerebral hemodynamics and cerebral blood volume: MR assessment using gadolinium contrast agents and T1-weighted Turbo-FLASH imaging. Am J Neuroradiol 1992;13:39–48.
25. Hackländer T, Reichenbach JR, Hofer M, Mödder U. Measurement of cerebral blood volume via the relaxing effect of low-dose gadopentetate dimeglumine during bolus transit. Am J Neuroradiol 1996;17:821–830.
26. Hackländer T, Hofer M, Reichenbach JR, Rascher K, Fürst G, Mödder U. Cerebral blood volume maps with dynamic contrast-enhanced T1-weighted FLASH imaging: Normal values and preliminary clinical results. J Comput Assist Tomogr 1996;20:532–539.
27. Hackländer T, Reichenbach JR, Modder U. Comparison of cerebral blood volume measurements using the T1 and T2* methods in normal human brains and brain tumors. J Comput Assisted Tomogr 1997;21:857–866.
28. Moody AR, Martel A, Kenton A, Allder S, Horsfield M, Delay G, Morgan P. Contrast-reduced imaging of tissue concentration and arterial level (CRITICAL) for assessment of cerebral hemodynamics in acute stroke by magnetic resonance. Invest Radiol 2000;35:401–411.
29. Larsson HB, Hansen AE, Berg HK, Rostrup E, Haraldseth O. Dynamic contrast-enhanced quantitative perfusion measurement of the brain using T1-weighted MRI at 3T. J Magn Reson Imag 2008;27:754–762.
30. Bruening R, Kwong KK, Vevea MJ, Hochberg FH, Cher L, Harsh IV GR, Niemi PT, Weisskoff RM, Rosen BR. Echo-planar MR determination of relative cerebral blood volume in human brain tumors: T1 versus T2 weighting. Am J Neuroradiol 1996;17:831–840.
31. Li KL, Zhu X, Waterton J, Jackson A. Improved 3D quantitative mapping of blood volume and endothelial permeability in brain tumors. J Magn Reson Imag 2000;12:347–357.
32. Lüdemann L, Hamm B, Zimmer C. Pharmacokinetic analysis of glioma compartments with dynamic Gd-DTPA-enhanced magnetic resonance imaging. Magn Reson Imag 2000;18:1201–1214.
33. Haroon HA, Buckley DL, Patankar TA, Dow GR, Rutherford SA, Balériaux D, Jackson A. A comparison of K^{trans} measurements obtained with conventional and first pass pharmacokinetic models in human gliomas. J Magn Reson Imag 2004;19:527–536.

34. Singh A, Haris M, Rathore D, Purwar A, Sarma M, Bayu G, Husain N, Singh Rathore RK, Gupta RK. Quantification of physiological and hemodynamic indices using T1 dynamic contrast-enhanced MRI in intracranial mass lesions. J Magn Reson Imag 2007;26:871–880.

35. Ostergaard L. Principles of cerebral perfusion imaging by bolus tracking. J Magn Reson. Imag 2005;22:710–717.

36. Sourbron S, Luypaert R, Van Schuerbeek P, Dujardin M, Stadnik T. Choice of the regularization parameter for perfusion quantification with MRI. Phys Med Biol 2004;49:3307–3324.

37. Jacquez JA. Compartmental analysis in biology and medicine. USA: The University of Michigan Press; 1985.

38. Brix G, Kiessling F, Lucht R, Darai S, Wasser K, Delorme S, Griebel J. Microcirculation and microvasculature in breast tumors: Pharmacokinetic analysis of dynamic MR image series. Magn Reson Med 2004;52:420–429.

39. Pradel C, Siauve N, Bruneteau G, Clement O, de Bazelaire C, Frouin F, Wedge S, Tessier J, Robert P, Frija G, Cuenod C. Reduced capillary perfusion and permeability in human tumour xenografts treated with the VEGF signalling inhibitor ZD4190: An in vivo assessment using dynamic MR imaging and macromolecular contrast media. Magn Reson Imag 2003;21:845–851.

40. Bazelaire C, Siauve N, Fournier L, Frouin F, Robert P, Clement O, Kerviler E, Cuenod C. Comprehensive model for simultaneous MRI determination of perfusion and permeability using a blood-pool agent in rats rhabdomyosarcoma. Eur Radiol 2005;15:2497–2505.

41. Tofts PS, Brix G, Buckley DL, Evelhoch JL, Henderson E, Knopp MV, Larsson HBW, Lee TY, Mayr NA, Parker GJM, Port RE, Taylor J, Weisskoff RM. Estimating kinetic parameters from dynamic contrast-enhanced T1-weighted MRI of a diffusible tracer: Standardized quantities and symbols. J Magn Reson Imag 1999;102:223–232.

42. Buckley DL, Kershaw LE, Stanisz G. Icellular-interstitial water exchange and its effect on the determination of contrast agent concentration in vivo: Dynamic contrast-enhanced MRI of human internal obturator muscle. Magn Reson Med 2008;60:1011–1019.

43. Larsson HBW, Rosenbaum S, Fritz-Hansen T. Quantification of the effect of water exchange in dynamic contrast MRI perfusion measurements in the brain and heart. Magn Reson Med 2001;46:272–281.

44. Lassen, NA, Perl WP. Tracer kinetic methods in medical physiology. New York: Raven Press; 1979.

45. Sourbron S, Michaely HJ, Reiser MF, Schoenberg SO. MRI-measurement of perfusion and glomerular filtration in the human kidney with a separable compartment model. Invest Radiol 2008;43:40–48.

46. Sourbron S, Dujardin M, Makkat S, Luypaert R. Pixel-by-pixel deconvolution of bolus-tracking data: Optimization and implementation. Phys Med Biol 2007;52:429–447.

47. Glatting G, Kletting P, Reske SN, Hohl K, Ring C. Choosing the optimal fit function: comparison of the akaike information criterion and the f-test. Med Phys 2007;34:4285–4292.

48. Ahearn TS, Staff RT, Redpath TW, Semple SIK. The use of the Levenberg-Marquardt curve-fitting algorithm in pharmacokinetic modelling of DCE-MRI data. Phys Med Biol 2005;50:N85–N92.

49. Stanisz GJ, Odrobina EE, Pun J, Escaravage M, Graham SJ, Bronskill MJ, Henkelman RM. T1, T2 relaxation and magnetization transfer in tissue at 3T. Magn Reson Med 2005;54:507–512.

50. Ito H, Kanno I, Kato C, Sasaki T, Ishii K, Ouchi Y, Iida A, Okazawa H, Hayashida K, Tsuyuguchi N, Ishii K, Kuwabara Y, Senda M. Database of normal human cerebral blood flow, cerebral blood volume, cerebral oxygen extraction fraction and cerebral metabolic rate of oxygen measured by positron emission tomography with 15O-labelled carbon dioxide or water, carbon monoxide and oxygen: A multicentre study in Japan. Eur J Nucl Med Mol Imag 2004;31:635–643.

51. Law I, Iida H, Holm S, Nour S, Rostrup E, Svarer C, Paulson OB. Quantitation of regional cerebral blood flow corrected for partial volume effect using O-15 water and PET. II. normal values and gray matter blood flow response to visual activation. J Cereb Blood Flow Metab 2000;20:1252–1263.

52. Pauliah M, Saxena V, Haris M, Husain N, Rathore RKS, Gupta RK. Improved T1-weighted dynamic contrast-enhanced MRI to probe microvascularity and heterogeneity of human glioma. Magn Reson Imag 2007;25:1292–1299.

53. Buckley DL, Roberts C, Parker GJM, Logue JP, Hutchinson CE. Prostate cancer: Evaluation of vascular characteristics with dynamic contrast-enhanced T1-weighted MR imaging–initial experience. Radiology 2004;233:709–715.

54. Herbert Koestler, Christian Ritter, Michael Lipp, Meinrad Beer, Dietbert Hahn, and Joern Sandstede. Prebolus quantitative MR heart perfusion imaging. Magn Reson Med 2004;52:296–299.